Title page

Highly sensitive acetone sensor based on WO_3 nanosheets derived from WS_2 nanoparticles with inorganic fullerene-like structures

Xueting Chang[1], Shuai Xu[1], Song Liu[2], Nannan Wang[2], Shibin Sun[1*], Xiaojie Zhu[1], Junfeng Li[1], Oluwafunmilola Ola[3], Yanqiu Zhu[4*]

[1] *College of Logistics Engineering, Shanghai Maritime University, Shanghai 201306, China*

[2] *Guangxi Institute Fullerene Technology (GIFT), Key Laboratory of New Processing Technology for Nonferrous Metals and Materials, Ministry of Education, School of Resources, Environment and Materials, Guangxi University, Nanning, China, 530004*

[3] *Faculty of Engineering, University of Nottingham, NG7 2RD, UK*

[4]*College of Engineering, Mathematics and Physical Sciences, University of Exeter, Exeter EX4 4SB, UK*

[*] Corresponding author: sunshibin@shmtu.edu.cn, Y.zhu@exeter.ac.uk.

Abstract

Metal oxide semiconductor (MOS) gas sensors are promising for applications in environmental monitoring, dangerous gas detection, and disease diagnosis. Seeking for advanced MOS sensing materials that possess high sensitivity and low limit of detection (LOD) at sub-ppm level is a great challenge. Here, we report the first creation of two-dimensional (2D) WO_3 nanosheets by annealing of the inorganic fullerene (IF)-like WS_2 nanoparticles that were prepared via sulfurization of WO_3 nanoparticles. Transformation of WS_2 to WO_3 was realised during the annealing process, simultaneously accompanied by the collapse of the hollow IF-WS_2 structures and the formation of tiny 2D WO_3 nanosheets with a lateral size of 40-80 nm. The resulting 2D WO_3 nanosheets exhibited highly enhanced acetone-sensing performance in terms of sensitivity, selectivity, and response/recovery rates compared with the WO_3 nanoparticles used as precursor for the synthesis of the IF-WS_2 nanoparticles. The nanosheets also demonstrated great repeatability, reliable long-term stability, and very low LOD, making them a promising candidate as gas sensor to detect breath acetone.

Keywords: Inorganic fullerene; WS_2 nanoparticles; WO_3 nanosheets; Gas sensors; Acetone-sensing.

1. Introduction

There are about more than 3,500 chemical components in exhaled breath, most of which are volatile organic compounds (VOCs) in trace quantities (below 1 ppm) [1, 2]. Breath analysis can monitor the abnormal variation of the breath VOCs, and thus it potentially offers an effective method for non-invasive disease diagnosis and health status monitoring [3-7]. Among the breath VOCs, acetone is a by-product of lipid metabolism and is closely related to the blood glucose level [8-10]. It is reported that the concentration of breath acetone from Type I diabetic patients are higher than 1.7 ppm, while the value for heathy individuals is in the range of 0.39-1.09 ppm [8, 11-13]. Additionally, breath acetone could be regularly measured to assess the burning of body built-up fat during exercise training and lifestyle interventions [14]. Therefore, breath acetone could not only be regarded as a validated biomarker for the early diagnosis of diabetic patients, but also could be used for monitoring individual's metabolic status [8]. To date, various techniques have been employed for measuring the breath acetone in very low concentration, such as gas chromatography-mass spectrometry [9], proton transfer reaction mass spectrometry [15], vacuum-free ion mobility spectroscopy [16], laser absorption spectroscopy [17], and colorimetric sensor [18]. However, these techniques require bulky equipment and complex measurement processes, therefore they are unable to realise real-time monitoring and cannot be widespread for individual uses. Hence, the development of a convenient and low-cost strategy for accurately detecting acetone at extremely low concentration is of high importance.

Metal oxide semiconductor (MOS) gas sensors have attracted tremendous interests in acetone sensing in recent years, owing to their high sensitivity, fast response, low cost, easy fabrication, and great potential of integration into portable devices [19-25]. Among various MOSs, tungsten oxides ($WO_{x\leq3}$) have gained special attention and are regarded as promising choices for acetone detection, because they exhibit features such as excellent chemical and physical stability, good controllability on structure, and strong reaction with VOCs [26, 27]. To achieve accurate detection of breath acetone in a gas sensor, two basic criteria should be satisfied: 1) the limit of detection (LOD) should be in the range of ppb level, especially under high humidity condition, and 2) having distinguished sensitivity towards acetone. For pure $WO_{x\leq3}$, only those with special modifications in composition,

crystalline structure, and morphology can satisfy the above requirements. For example, Wei *et al.* fabricated the daisy-like hexagonal WO_3 nanostructure with exposed (002) facets using a hydrothermal method with $Na_2WO_4 \cdot H_2O$ and HCl as raw materials [28]. Since the (002) facets were highly favourable for the adsorption of acetone, the daisy-like WO_3 nanostructure exhibited high sensitivity and remarkable reproducibility towards sub-ppm level acetone (0.2-1 ppm). Inspired by the accelerated oxidation process of metals in marine water containing high concentration of NaCl, Galstyan *et al.* established a green approach for preparing the monoclinic γ-WO_3 nanomaterial by annealing the tungsten thin film in NaCl aqueous solution in a Teflon liner at 160 ºC for 20 h [29]. Due to the catalytic activity and large dipole moment, the γ-WO_3 nanomaterial exhibited a LOD of 170 ppb towards acetone and a stable acetone-sensing performance at 20-80% of relative humidity (RH). Lu *et al.* prepared the monoclinic WO_3 nanos with oxygen vacancies via a microwave-assisted hydrothermal technique, and the WO_3 nanocrystalline has been found to exhibit outstanding high sensitivity to 0.25-500 ppm of acetone and a very low detection limit of 7.5 ppb [30]. Imran *et al.* prepared the porous WO_3 nanofibers through electrospinning polyvinylpyrrolidone (PVP) nanofibers embedded with WO_3 nanoparticles and subsequent annealing in air [31]. With the assistance of light irradiation and applying a bias voltage, the porous WO_3 nanofibers demonstrated ppb-level detection limit.

Two-dimensional (2D) nanostructures, such as graphene [32, 33], Mxene [34-36], and transition metal dichalcogenides of WS_2 and NbS_2 [37-40], are recently emerged as sensing materials for gas sensors, due to advantages of high specific surface area, adequate active sites, and unique electronic properties. However, because of the strong covalent interaction between interlayers in a WO_3 crystal, the synthesis of 2D WO_3 nanostructures via process such as the exfoliation of bulk WO_3 is challenging. A possible way to produce the 2D WO_3 nanostructures is by direct oxidation of the 2D WS_2 nanosheets, which can be easily exfoliated from bulk WS_2 powder. Adigilli *et al.* attempted the oxidation process and resulted in 2D WS_2/WO_3 heterostructures, 2D WO_3 nanosheets (~ 10 nm thick), and spherical WO_3 nanoparticles under different annealing conditions [41]. Azam *et al.* fabricated highly-crystalline 2D WO_3 nanosheets with a lateral size of ~20 μm and thickness below 10 nm via a similar oxidation of 2D WS_2 nanosheets [42]. Yim *et al.* prepared the 2D PdO/WO_3

nanohybrids through direct conversion of metallic WS_2 nanosheets to ultrathin 2D WO_3 nanosheets and simultaneous deposition of PdO nanoclusters on the sheet surface [43]. The 2D PdO/WO_3 nanohybrids excellent photocatalytic activity and repeatability for Suzuki cross-coupling reactions under visible light irradiation. F. Perrozzi *et al.* fabricated the 2D WS_2/WO_3 composite by annealing the WS_2 flakes at 150-350 ºC [44]. They found that the 2D WS_2/WO_3 composites exhibited excellent gas sensing performance to H_2, NH_3, and NO_2 at a low working temperature of 150 ºC. Besides the 2D WS_2 nanosheets, WS_2 nanoparticles with inorganic fullerene-like structures (IF-WS_2) could be alternative precursor for the synthesis of 2D WO_3 nanosheets. IF-WS_2 nanoparticles, having hollow-caged onion-like structures, are excellent solid-state lubricants and super shock absorbers [45, 46]. It is possible that 2D WO_3 nanostructures may be formed once the IF-WS_2 cages are collapsed during the oxidation processes.

This work validates the above hypnosis. We report the first creation of 2D WO_3 nanosheets through annealing of the IF-WS_2 nanoparticles in air, investigate their transition mechanism and demonstrate the excellent VOCs sensing performance of the resulting 2D WO_3 nanosheets.

2. Experimental

2.1 Chemical reagent

Acetone, ethanol, ammonia, formaldehyde, isopropanol, and carbon disulfide were purchased from Sinopharm Chemical Reagent Co. Ltd. Purified water was prepared by using a UPW-N300UV water purifier (Shanghai INESA Scientific Instrument Co., Ltd.). Commercial WO_3 nanoparticles (NPs) with sizes of 40-60 nm and purity of 99% were supplied by Zhejiang Manli Nano Technology Co. Ltd. Commercial 2D WS_2 nanoparticles were provided by Nanjing XFNANO Materials Tech Co. Ltd.

2.2 Synthesis of IF-WS_2 nanoparticles

The IF-WS_2 nanoparticles were synthesized by using a home-made rotary furnace, as has been described in our previous work [47, 48]. Firstly, 10 g of WO_3 nanoparticles was placed at the center of the quartz tube in the self-made high-temperature horizontal rotary furnace. Following flushing the quartz tube with Ar gas (100 mL/min) for 30 min, the furnace was heated to 800 ºC at a heating rate of 5 ºC min^{-1}. Then, H_2S gas flow took place at a flow rate of 12 mL/min. After reaction for 2 h,

the H_2S gas flow was shut off and the heating was stopped. After cooling the quartz tube down to room temperature under Ar gas flow, the IF-WS_2 nanoparticles were obtained.

2.3 Purifying of IF-WS_2 nanoparticles

The as-obtained IF-WS_2 nanoparticles were transferred to a beaker containing 50 mL carbon disulfide for ultrasonic treatment for 30 min. Subsequently, the IF-WS_2 nanoparticles were washed twice with purified water and then centrifuged with ethanol for collection. Finally, the IF-WS_2 nanoparticles was dried in an oven at 60 ºC for 2 h.

2.4 Annealing of IF-WS_2 nanoparticles

The as-purified IF-WS_2 nanoparticles were annealed at temperatures ranging from 150 to 550 ºC in a muffle furnace. The heating rate of the furnace was 10º/min and the heating time at desired temperature was 4 h. After finishing the heating process, the samples in the furnace were naturally cooled to room temperature. For convenience, the IF-WS_2 nanoparticles annealed at 150 ºC, 250 ºC, 350 ºC, 400 ºC, 450 ºC, 500 ºC, and 550 ºC were designated as WS_2-150, WS_2-250, WS_2-350, WS_2-400, WS_2-450, WS_2-500, and WS_2-550, respectively.

2.5 Characterization

The X-ray diffraction (XRD) patterns of the as-prepared samples were acquired on an X-ray diffractometer (D/MAX-2500, Rigaku, Japan), with a Cu-Kα radiation (λ=1.5418 Å) over a 2θ range of 5-90º. The morphology of the samples was characterized by scanning electron microscopy (SEM) on a Quanta Q400 microscope (FEI, USA) operated at 20 kV and by transmission electron microscopy (TEM) on a Tecnai G2 F30 microscope (FEI, USA) operated at 200 kV. Energy-dispersive spectroscopy (EDS) mapping images were taken on a Genesis spectrometer (EDAX, USA). X-ray photoelectron spectroscopy (XPS) analysis was carried out on an ESCALAB 250Xi spectrometer (Thermo Fisher Scientific, USA) using a monochromatic Al K_α source (1486.6 eV).

2.6 Gas-sensing measurements

Different sensing materials including the WO_3 nanoparticles, unannealed and annealed IF-WS_2 nanoparticles were dispersed in purified water under sonication for 10 min. The suspensions were then deposited onto a ceramic tube with two Au electrodes to form the sensing film. The gas-sensing

measurements were performed on a WS-30A system (Zhengzhou Winsen Electronics Technology Co., Ltd). Various VOCs, including acetone, ethanol, ammonia, formaldehyde, and isopropanol, were used as the target gases, and their solvents were injected into a sealed chamber of 18 L using a microsyringe, which were then heated to form their individual vapors. The sensors were exposed to different vapors with concentrations in the range of 0.17-500 ppm. After the resistance of the sensor reached a stable stage, the chamber was rapidly opened to allow the vapors to be discharged to the ambient air. The working temperature of the sensors was controlled by adjusting the voltage of the Ni-Cr heating wire that was inserted into the ceramic tube. The sensor response was defined by R_a/R_g, where R_a and R_g are the resistances of the sensor exposed in the ambient air and in the target gases, respectively. The response and recovery times of the sensor were determined as the time taken to achieve 90% change of the resistance during the gas injecting and discharging processes, respectively.

The effects of relative humidity (RH) on the gas-sensing activities of the gas sensors were also studied. The RH in the test chamber was regulated to be in the range of 30%-90% at room temperature (~26 ºC). A high-precision hygrometer was placed in the chamber to monitor the RH. After the RH reached the acquired value, the gas-sensing measurements were carried out.

3. Results and Discussion

3.1 Synthesis mechanism of WO_3 nanosheets

The synthesis process of the WO_3 nanosheets with ultrafine sizes from the IF-WS_2 nanoparticles is illustrated in Fig. 1. The preparation of the WO_3 nanosheets involves two steps, *i.e.* the conversion of WO_3 nanoparticles to IF-WS_2 nanoparticles by solid-gas reaction and the subsequent annealing oxidation of the IF-WS_2 nanoparticles. At the early stage of the first step, the surfaces of the WO_3 nanoparticles (Fig. 1a) reacted with H_2S gas, leading to the growth of a WS_2 shell consisting of few WS_2 atomic layers, as shown in Fig. 1b. Then, sulfur diffused slowly into the core and converted the core oxide into sulphide. After sulfidization reaction for 2 h, the IF-WS_2 nanoparticles with hollow structure were obtained (Fig. 1c). It should be noted that the WO_3 nanoparticles used as precursor should have sizes of < 200 nm, otherwise WS_2 platelets rather than IF-WS_2 nanoparticles could be predominately obtained [49]. Herein, the WO_3 nanoparticles possessed quasi-spherical morphologies

with sizes of 40-160 nm (Fig. S1a), which exactly qualifies the requirement for the formation of the IF-WS_2 nanoparticles. In the following annealing process (step 2), oxidation of the surfaces of IF-WS_2 nanoparticles would occur firstly, forming the WS_2/WO_3 heterostructures, see Fig. 1d. Given the unique hollow structures of IF-WS_2 nanoparticles, they may probably swell under thermal processing. This means that swelling of the IF-WS_2 nanoparticles and sulphide-to-oxide conversion occurred concurrently. Since the WS_2 and WO_3 exhibited not only different thermal expansion coefficients but also crystalline structures, the annealing process could result in both thermal stress and deformation stress within the WS_2/WO_3 heterostructures. With the proceeding of the oxidation process outside in, the stress in the hollow nanoparticles would increase gradually. One can image that the hollow structure would crack when the stress reached a critical value, leading to the formation of the WS_2 nanosheets and the WO_3 nanosheets that were adhered to the WS_2/WO_3 heterostructures, as seen in Fig. 1e. The cracking of the hollow spheres may occur simultaneously at different sites. The crack would further propagate under the thermal and deformation stresses, resulting in the complete collapse of the cracked cages. Finally, WO_3 nanosheets (Fig. 1f) were generated after the complete conversion of sulphide to oxide.

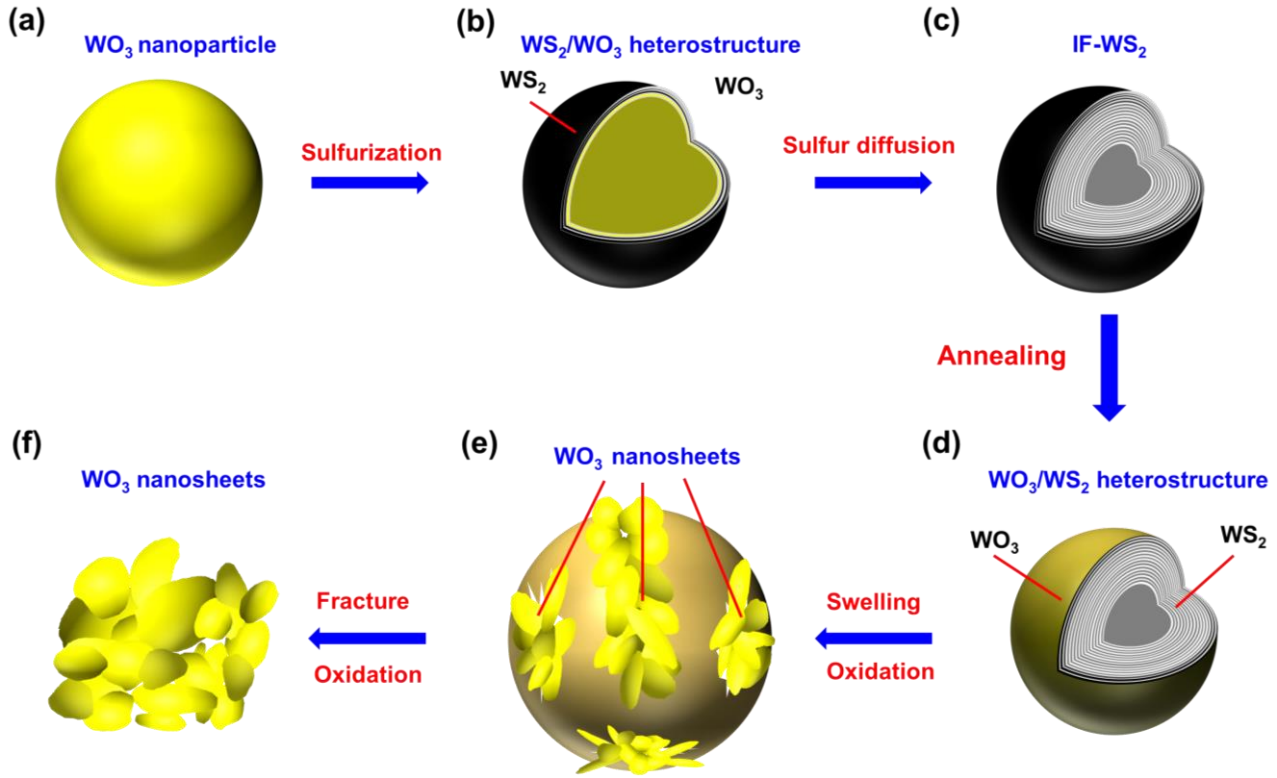

Fig. 1. Schematic of synthesis process of the WO_3 nanosheets.

3.2 Characterization

Fig. 2a shows the XRD patterns of the pure IF-WS_2 and annealed IF-WS_2 nanoparticles. The main diffraction peaks of the IF-WS_2 nanoparticles occurred at 14.3º, which corresponds to the (002) plane of hexagonal WS_2. No impurity peaks are visible, indicating the high purity of the IF-WS_2 nanoparticles. The XRD patterns of the WS_2-150 and WS_2-250 were identical to that of the IF-WS_2 nanoparticles, suggesting that no noticeable reaction occurred when temperature was lower than 250 ºC. As for the WS_2-350, annealing at 350 ºC, the diffraction peaks arising from WO_3 became evident, which is indicative of the formation of WO_3 from the oxidation of WS_2. WO_3 was predominated in sample WS_2-400, accompanied with traces of WS_2. As seen from the EDS spectra, a small portion of S element can be found in samples WS_2-350 (Fig. S2a) and WS_2-400 (Fig. S2b), whilst W and O signals are intense. This result shows that both the WS_2-350 and WS_2-400 were a combination of WS_2 and WO_3, *i.e.* the WS_2/WO_3 heterostructures. All diffraction peaks of sample WS_2-450 have been indexed to monoclinic WO_3, matching well with that no S was detected in the EDS spectra (Fig. S2c), which confirms the complete transition from WS_2 to WO_3 after annealing at 450 ºC for 4 h. The diffraction peaks at 23.2º, 23.6º, and 24.1º correspond to the (002), (020), and (200) planes of monoclinic WO_3, respectively. The diffraction peaks associated with WO_3 for the WS_2-450 were sharper than those of the WS_2-400, indicative of the higher crystallinity of the former. The XRD patterns of samples WS_2-500 and WS_2-550 were almost identical to that of the WS_2-450, confirming that IF-WS_2 became pure WO_3 after annealing at temperatures higher than 450 ºC, which is in accordance with previous reports [41, 44]. Actually, the WO_3 nanoparticles used as precursor for the synthesis of the IF-WS_2 nanoparticles exhibited monoclinic structures (Fig. S1b), which was identical to those of the WS_2-450, WS_2-500 and WS_2-550. As seen from the enlarged area in Fig. 2a, the relative intensity of the (002) diffraction peaks is slightly higher than those of the (020) and (200) diffraction, revealing that the WO_3 has a preferred crystal face growth of (002) plane [28]. In addition, the diffraction peaks for samples WS_2-350 and WS_2-400 were obviously shifted towards lower diffraction angles, compared with other samples, which can be attributed to the deviation of the oxygen atoms in WO_3 caused by the existence of the WS_2 [42, 50].

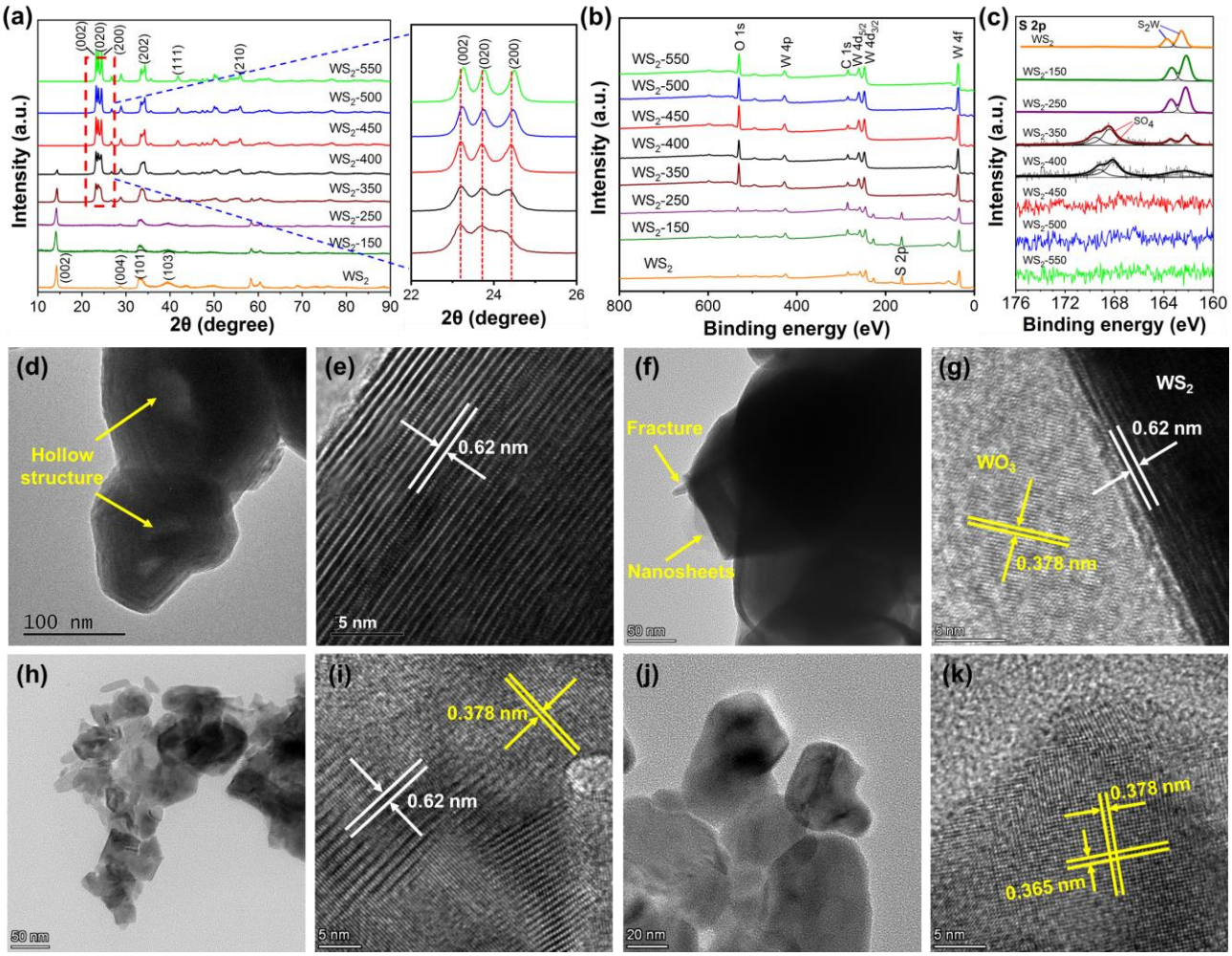

Fig. 2. (a) XRD patterns and (b) Survey XPS spectra for pure IF-WS_2 and annealed IF-WS_2 at different temperatures. (c) S 1s and their corresponding deconvoluted spectra for different samples. TEM images of (d, e) IF-WS_2, (f, g) WS_2-250, (h, i) WS_2-400, and (j, k) WS_2-500.

The transformation process from WS_2 to WO_3 by annealing was further investigated by using XPS. Fig. 2b shows the survey XPS spectra of the unannealed and annealed IF-WS_2 nanoparticles. In addition to the peaks associated with W and S, a very weak peak belonging to O was detected for the IF-WS_2 nanoparticles, which can be attributed to the slight oxidation of WS_2 in air. Similar phenomenon happened in the survey XPS spectra of both the WS_2-150 and WS_2-250. Though WS_2 was retained in the WS_2-350 and WS_2-400, as proved by the XRD results, no obvious peaks corresponding to S were detected from the survey XPS spectra, indicative of the strong surface oxidation under these conditions. Fig. 2c shows the evolution of the S 2p core-level spectra for

different samples as a function of annealing temperature, which provided further evidence for this phenomenon. The S 2p core-level spectrum for the IF-WS_2 nanoparticles, WS_2-150, and WS_2-250 could be deconvoluted into two peaks located at 162.61 and 163.76 eV, which can be ascribed to the S $2p_{3/2}$ and S $2p_{1/2}$ states, respectively. As for samples WS_2-350 and WS_2-400, the peak corresponding to SO_4^{2-} state (168.48 eV) appeared, which may arise from the formation of the WS_2/WO_3 heterostructures. The SO_4^{2-} ions were usually found on the surfaces of WS_2 exposed to air or annealed WS_2 [44]. When annealing at temperature higher than 450 ºC, no peaks for S 2p can be detected, confirming the complete conversion from WS_2 to WO_3.

The morphologies of the unannealed and annealed IF-WS_2 nanoparticles were firstly identified by SEM. As shown in Fig. S3a and S3b, most of the particles constituting the samples IF-WS_2 and WS_2-150 exhibited quasi-spherical structures with sizes of 80-200 nm. The overall shapes of the IF-WS_2 nanoparticles and WS_2-150 were quite similar to those of the WO_3 precursor (Fig. S1a), but their sizes increased slightly after the sulfidization step. After annealing at temperatures of 350-550 ºC, pronounced morphological changes happened, which directly verifies the damage of the close-caged hollow structures of the IF-WS_2 nanoparticles. As shown in Fig. S3c-3f, layered structures occurred in the WS_2-350, WS_2-400, WS_2-450, and WS_2-500, and the single layer was found to be composed of a great number of ultrafine sheet-like nanoparticles. However, the layers were stacked together, making it impossible to discern the definite structure of the annealed samples.

TEM was further employed to identify the morphologies of different samples. In Fig. 2d and Fig. S4a, the IF-WS_2 nanoparticles exhibited hollow-caged structures, *i.e.* fullerene-like structures. HRTEM images (Fig. 2e and Fig. S4b) show that the IF-WS_2 nanoparticles generally consisted of 30-40 layers (that varies with the sizes of the nanoparticles), and the layer-to-layer distance was measured to be 0.62 nm. The WS_2-150 exhibited similar morphology to that of unannealed IF-WS_2 nanoparticles, but a thin WO_3 films was formed on its surface (Fig. S5a and S5b), which reveals the early surface oxidation at 150 ºC. After annealing at 250 ºC, slight damages occurred to the cage structure whilst WO_3 nanosheets adhered to it were formed, as indicated in Fig. 2f and 2g. Increasing the temperature to 350 ºC and 400 ºC, the IF-WS_2 nanoparticles underwent a pronounced morphological change. As shown in Fig. S6a and 2h, the fullerene-like structures disappeared and

irregular nanosheets formed. In Fig. S6b and 2i, the distances of the lattice fringes were measured as 0.62 and 0.378 nm, which correspond to the inter-planar spacings of the (002) planes in hexagonal WS_2 and (020) planes in monoclinic WO_3, respectively. Both the WS_2-450 (Fig. S7) and WS_2-500 (Fig. 2j) were composed of tiny nanosheets with length of 40-80 nm. Considering the IF-WS_2 nanoparticles had large sizes of 80-200 nm, we can deduce that one IF-WS_2 nanoparticle was transformed to a few WO_3 nanosheets, via cracking during the collapse of the cages. The clear lattice fringe shown in Fig. 2k verifies the high crystallinity of the resulting WO_3 nanosheets, with lattice distances of 0.378 and 0.365 nm corresponding to (020) and (200) planes of the monoclinic WO_3, respectively [28, 51]. This result also reveals that the exposed faces in the WO_3 nanosheets are dominantly the (002) planes, in agreement with the XRD result. Actually, the monoclinic WO_3 crystals with exposed (002) planes are much stable because the (002) plane has the lowest energy [52, 53]. Therefore, the oxidation of the IF-WS_2 nanoparticles accompanied with the collapse of their hollow structures tended to generate the WO_3 nanosheets with dominantly-exposed (002) planes. As shown in Fig. S8a, large and thick WO_3 nanosheets appeared in the WS_2-550, which should be attributed to the coalescence of the WO_3 nanosheets during annealing. A HRTEM image shown in Fig. S8b proves that a few nanosheets were stacked together.

3.3 Acetone-sensing performance

Fig. 3a-3e shows the response-recovery characteristics of different sensors towards 50 ppm of acetone at varied temperatures. The resistance of both the WS_2 and WS_2-350 sensors showed very slight change upon exposing to 50 ppm of acetone (Fig. S9), which reveals that these materials showed negligible responses to acetone. By contrast, the resistance of the other four samples, *i.e.* the WO_3, WS_2-400, WS_2-450, WS_2-500, and WS_2-550, decreased abruptly upon exposure to acetone. This confirms that they were sensitive to acetone and behaved as n-type sensing behavior. Their response/recovery behaviors were significantly influenced by the working temperature. Taking sample WS_2-500 as an example, its response/recovery times was 24/106 s at a low working temperature of 200 ºC, which reduced significantly to 7/30 s and 7/13 s as the temperature increased to 250 ºC and 300 ºC, respectively, as presented in Fig. S10. At 350 ºC, sample WS_2-500 possessed the fastest response/recovery times of 5/8 s. When the temperature reached 400 ºC, the response time

remained constant but the recovery time increased largely to 15 s.

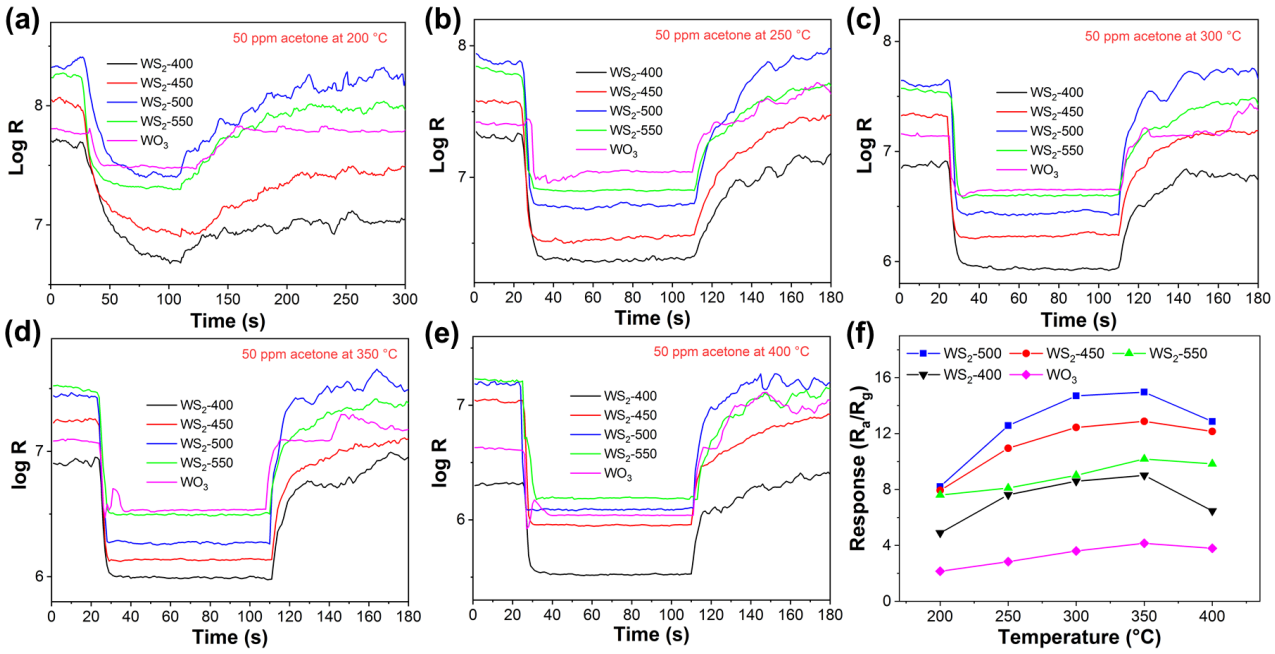

Fig. 3. Response-recovery characteristics of different sensors exposed to 50 ppm of acetone at working temperature of (a) 200 ºC, (b) 250 ºC, (c) 300 ºC, (d) 350 ºC, and (e) 400 ºC. (f) Plots of responses for different sensors towards 50 ppm of acetone as a function of working temperature.

Besides response/recovery times, the responses of the sensors also depended strongly on the working temperature. Fig. 3f plots the responses of the sensors to 50 ppm of acetone as a function of working temperature. The responses of the sensors increased firstly with increasing working temperature and then decreased when the temperature exceeds 350 ºC. Additionally, the responses measured at 300 ºC were highly comparable to those measured at 350 ºC. Considering the response and recovery features, we believe that their optimum working temperature should be in the range of 300-350 ºC. It is generally accepted that the working temperature could not only determine the reaction kinetics of both the acetone molecule and oxygen ion species (O_2^-, O^-, and O^{2-}) adsorbed on the sensing materials, but also influence the diffusion rate of the acetone molecules [54]. Low working temperature means weak reaction between acetone and oxygen ion species and low diffusion rate of acetone, which results in poor response and low response/recovery rates. Moreover, the desorption of the adsorbed acetone molecules from the sensing materials was inhibited at low temperature. As a result, the resistance of the sensors cannot return to the original values after

acetone was discharged (Fig. 3a). Too high temperature is also detrimental to the sensing performance of the sensors because the diffusion rate (or desorption rate) of the acetone molecules was too high to react effectively with the oxygen ion species. Among the sensors sensitive to acetone, the WS_2-500 sensor owned the highest responses over the whole working temperature. The response of the WS_2-500 sensor towards 50 ppm of acetone at 300 ºC was 14.7, which was 1.18, 1.63, 1.7, and 4.1 times higher than those of samples WS_2-450 (12.4), WS_2-550 (9.0), WS_2-400 (8.6), and WO_3 (3.6), respectively. It is worth mentioning that the responses of WS_2-400, WS_2-450, WS_2-500, and WS_2-550 sensors were much higher than those of the WO_3 sensor. These results have validated that the present WO_3 nanosheets obtained via oxidation of IF-WS_2 nanoparticles exhibit highly enhanced sensitivity against WO_3 nanoparticles.

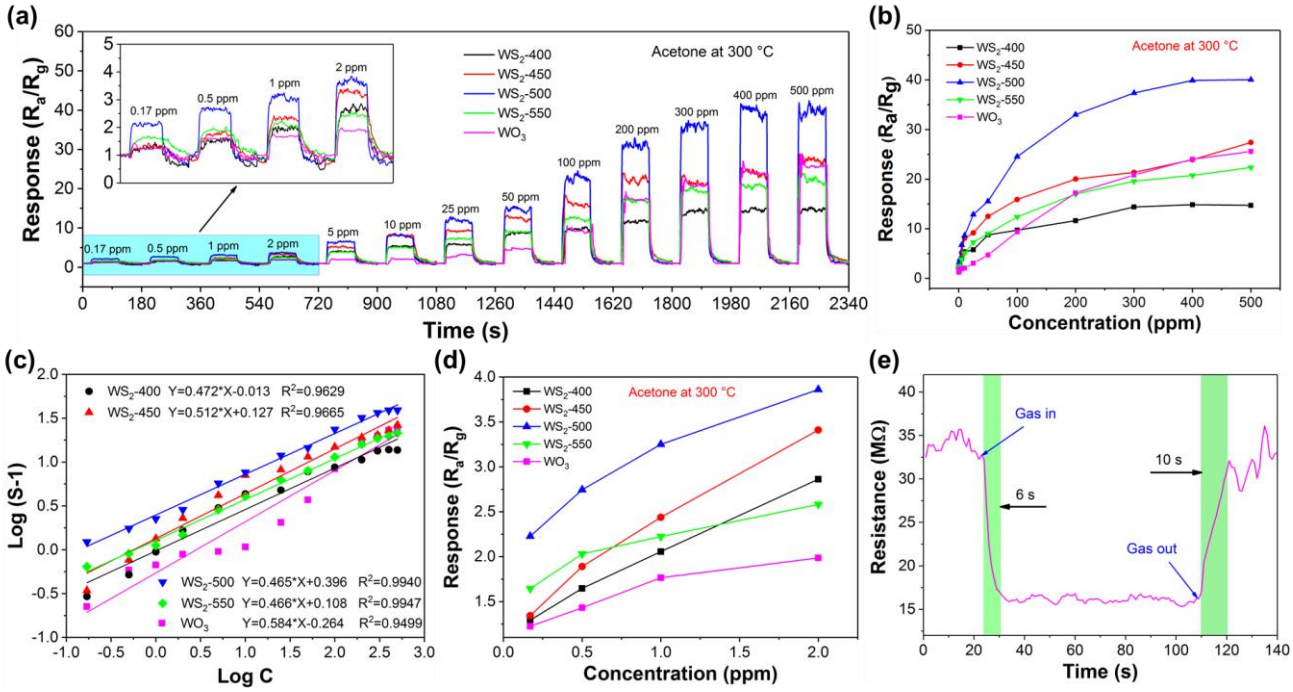

Fig. 4. (a) Dynamic response-recovery curves of different sensors to increasing acetone concentrations from 0.17 to 500 ppm at 300 ºC. Inset in (a) is the enlarged curves towards 0.17-2 ppm of acetone. (b) Plots of responses for different sensors as a function of acetone concentration (0.17-500 ppm). (c) Response-concentration relationships of different sensors. (d) Plots of responses for different sensors as a function of acetone concentration (0.17-2 ppm). (e) Response and recovery times of (d) WS_2-500 sensor towards 0.17 ppm of acetone.

We further investigated their acetone-sensing performance by varying the acetone concentrations from 0.17 to 500 ppm. Since samples WS_2 and WS_2-350 showed no response to acetone, we only focused our attention on samples WO_3, WS_2-400, WS_2-450, WS_2-500, and WS_2-550. Fig. 4a shows their dynamic gas responses to various concentrations of acetone at 300 ºC. All samples exhibited noticeable responses to acetone over the whole testing concentrations, whilst sample WS_2-500 showed the highest responses towards both the low-concentration and high-concentration. As plotted in Fig. 4b, the responses of sample WS_2-500 increased continuously with increasing acetone concentrations until 400 ppm, demonstrating an impressively wide detecting range. By contrast, the responses of samples WS_2-400, WS_2-450 and WS_2-550 increased slowly with the concentration exceeding 200 ppm.

Normally, the relationship between the response (R_g) and gas concentration (C_g) of a MOS sensor can be expressed by the following equation:

$$R_g=1+\alpha C_g^{\beta} \quad (1)$$

where is α is prefactor, and β is the charge parameter of surface species [55-58]. The equation (1) can be rewritten in a linear form:

$$\log(R_g-1)=\beta\log(C_g)+\log\alpha \quad (2)$$

By processing the data shown in Fig. 4b, the $\log(R_g-1)$ *vs* $\log(C_g)$ curves for different sensors can be obtained, as shown in Fig. 4c. The R^2 values of the WS_2-500 and WS_2-550 sensors are >0.99, indicating that their responses to acetone have perfect linear relationship with the testing range. By contrast, the WO_3 and WS_2-400 sensors demonstrated a very poor linear relationship. The β values of the WO_3, WS_2-400, WS_2-450, WS_2-500, and WS_2-550 sensors were determined to be 0.584, 0.472, 0.512, 0.465, and 0.466, respectively. As reported, the β values are 0.5 and 1 when the adsorbed oxygen species are O^{2-} and O^-, respectively [59]. Thus, we attribute that the adsorbed oxygen species on the surfaces of all the sensing materials are mainly O^{2-}.

The ability to detect ultralow acetone concentration (below 1 ppm) is of vital importance for the gas sensors in diagnosing early diabetic patients. We are delighted to report that all the tested sensors demonstrated surprisingly good responses towards acetone at a concentration as low as 0.17 ppm

(inset in Fig. 4a). Notably, the WS_2-500 sensor showed outstanding and relatively stable response, important indicators for being safely employed to detect ultralow content of acetone. Fig. 4d denotes the sensing responses to 0.17-2 ppm of acetone. The WS_2-500 sensor exhibited a response of 2.23 towards 0.17 ppm of acetone, which exceeds most of the previously reported values of the acetone sensors based on the WO_3 nanomaterials [22, 60-64]. As for the WO_3, WS_2-400, WS_2-450, and WS_2-550 sensors, the responses towards 0.17 ppm of acetone were much lower, which were 1.22, 1.29, 1.34, and 1.64, respectively. Since the minimum acetone concentration can be set to be only 0.17 ppm in the dilution system, the theoretical LOD for the WS_2-500 sensor should be much lower. The theoretical LOD of the WS_2-500 sensor can be calculated according to the equation (3) [65-68]:

$$LOD = 3\sigma/S_L \quad (3)$$

where σ denotes the standard deviation of the background signal of the sensor in air, and S_L was the slope of the fitting line of the response-concentration curve (Fig. 4d). Calculation reveals that the WS_2-500 sensor owned a very low theoretical LOD of 0.029 ppm (29 ppb), which can fully meet the requirement for detecting sub-ppm-level acetone. Furthermore, the WS_2-500 sensor presented very fast response and recovery times of 6 and 9 s towards 0.17 ppm of acetone (Fig. 4e), respectively, which were comparable to those towards 50 ppm of acetone.

Based on the above discussions, the WS_2-500 sensor demonstrated the best acetone-sensing performance in terms of sensitivity and response/recovery rates, making it encouraging candidate for acetone sensor. For practical application, the stability of the WS_2-500 sensor and the influence of RH on its acetone-sensing performance should be considered. We investigated the stability and repeatability of the WS_2-500 sensor by repeatedly sensing 50 ppm of acetone for 100 cycles at 300 ºC. As shown in Fig. 5a, the cyclic response-recovery curves were repeatable and stable, without response degradation, demonstrating the remarkable stability and repeatability. The long-term stability of the WS_2-500 sensor was also assessed by measuring its response every 2 days over a period of 2 weeks. As shown in Fig. S11, there is no obvious variation on the responses of the WS_2-500 sensor after 14 days of testing, verifying its trustworthy long-term stability. The response-recovery curves of the WS_2-500 sensor to 50 ppm of acetone at 300 ºC under different RH are shown in Fig. 5b. Fig. 5c presents the plot of responses of the WS_2-500 sensor to 50 ppm of

acetone at 300 ºC as a function of RH. Obviously, the RH had negligible influence on the response of the WS_2-500 sensor when the RH was in the range of 40-60%. However, the response of the WS_2-500 sensor decreased dramatically with increasing RH when the RH was higher than 60%. At 80% RH, the response was 7.18, which is 2.17 times lower than that (15.46) measured at 30% RH. This should be due to the fact the water molecules could compete with both the oxygen and acetone molecules to occupy the active sites of the sensing materials during the sensing process, which would then deteriorate the reaction between the acetone and oxygen ion species [69, 70]. Correspondingly, the response of the WS_2-500 sensor towards acetone decreased with increasing RH especially when the RH was very high (>60%).

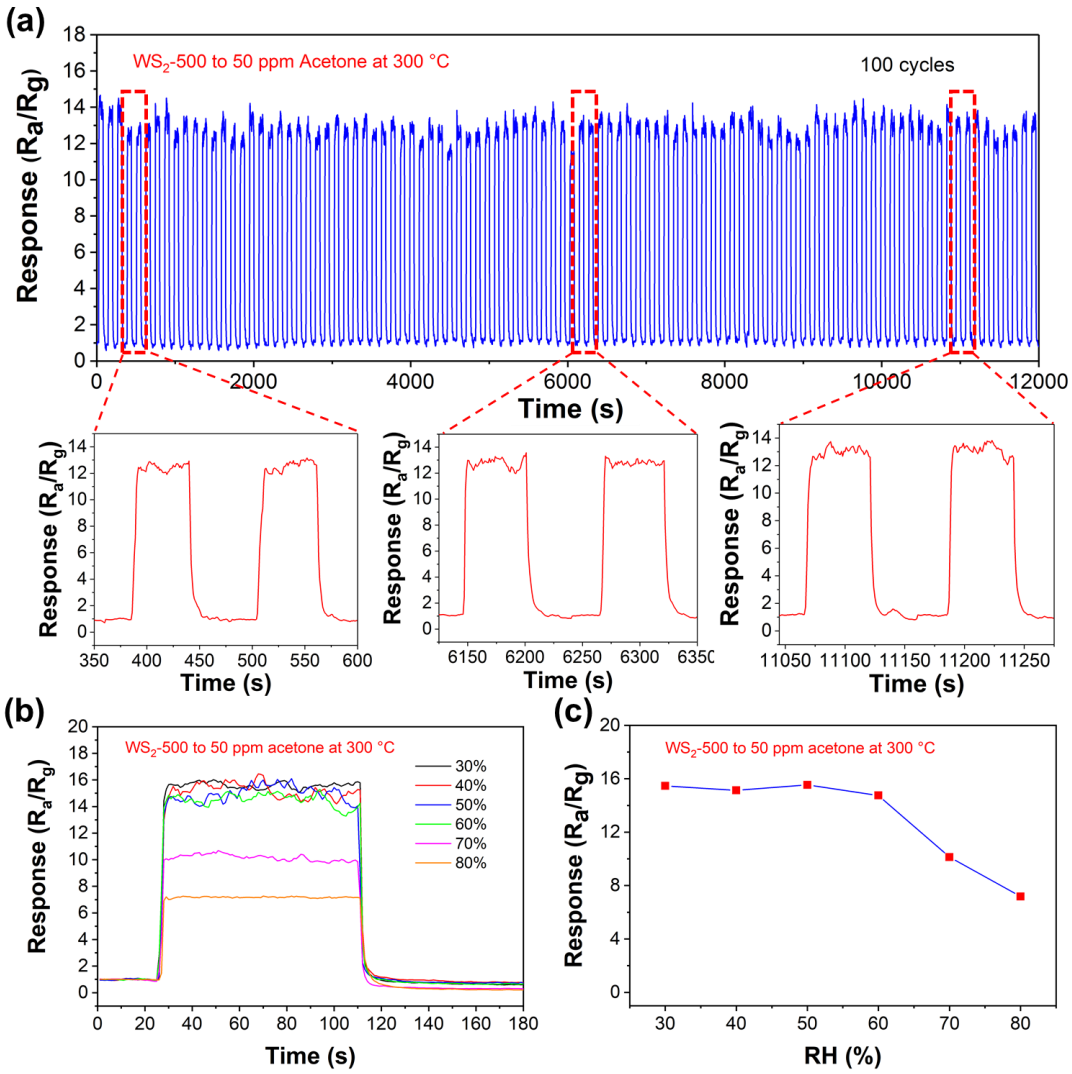

Fig. 5. (a) Response-recovery curves of WS_2-500 sensor for 100 cycles to 50 ppm of acetone at 300 ºC. (b) Response-recovery curves of WS_2-500 sensor to 50 ppm of acetone at 300 ºC under different RH and (c) plot of response as a function of RH.

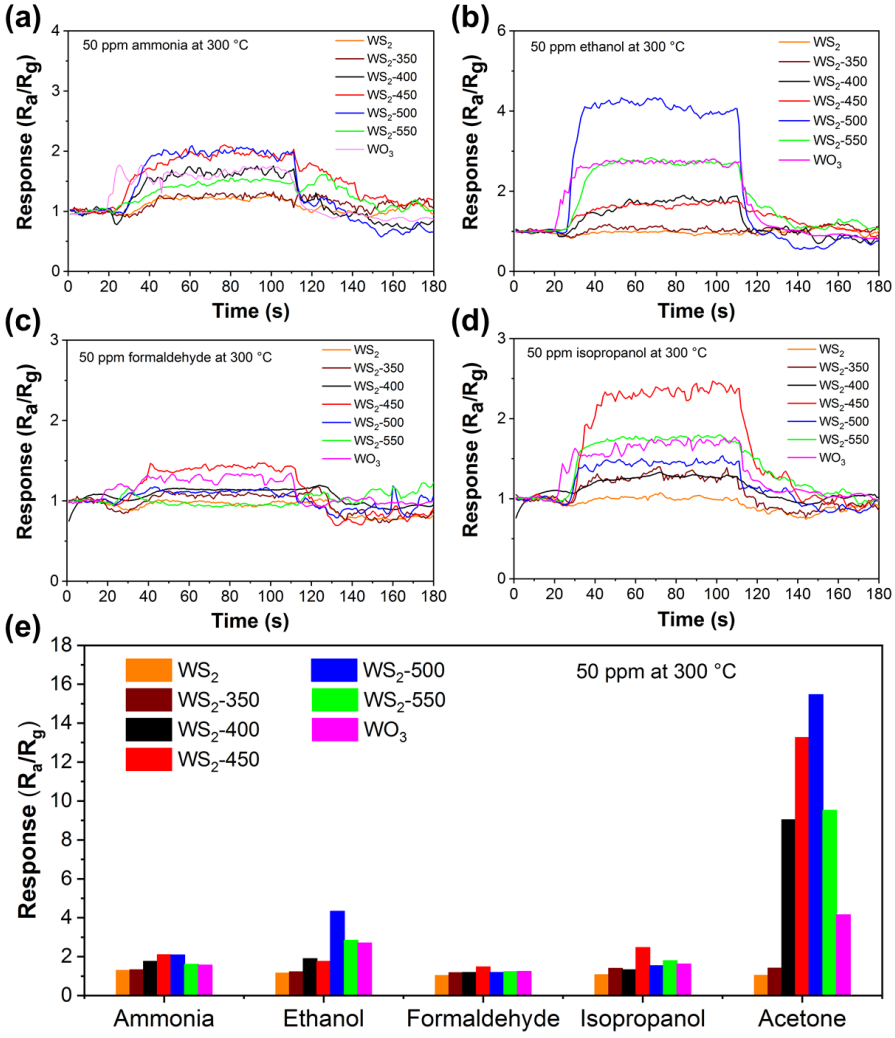

Fig. 6. Response-recovery curves of different sensors to (a) ammonia, (b) ethanol, (c) formaldehyde, and (d) isopropanol at 300 ºC. (d) Responses of different sensors to different gases at a concentration of 50 ppm.

To examine the selectivity of different sensors, their responses towards some typical VOCs including ammonia, ethanol, formaldehyde, and isopropanol were measured. Fig. 6a-6d shows the response-recovery curves of different sensors to 50 ppm of the targeted gases at 300 ºC. The WS_2 sensor showed negligible responses to all the tested gases, while the WS_2-350 sensor displayed only negligible responses to ammonia and ethanol, and very slight responses to formaldehyde and isopropanol. This suggests that these two sensors cannot be used as gas sensor for detecting VOCs. Despite observable responses occurred for the WO_3, WS_2-400, WS_2-450, WS_2-500, and WS_2-550 sensors when sensing the targeted gases, the values were relatively small. Fig. 6e illustrate the

comparison of responses of different sensors to different gases. Apparently, the responses of the WS_2-400, WS_2-450, WS_2-500, and WS_2-550 sensors towards acetone were much higher than those towards other gases, confirming their selectivity for acetone. For example, the response (14.96) of the WS_2-500 sensor towards acetone was 7.15, 3.45, 12.67, and 9.77 times higher than those towards ammonia (2.09), ethanol (4.33), formaldehyde (1.18), and isopropanol (1.53) under the same conditions. In comparison, the WO_3 sensor exhibited poor selectivity because it demonstrated similar responses to acetone and ethanol and indiscriminate responses to the other tested VOCs.

3.4 Acetone-sensing mechanism

The acetone-sensing mechanism of the typical n-type WO_3 is illustrated in Fig. 7a. When the WO_3 is exposed to air, the oxygen molecules will be adsorbed onto their surfaces and then capture the electrons from the conductance band of WO_3 to form the oxygen ion species including O_2^-, O^-, and O^{2-} [27, 71, 72]. Herein, the main adsorbed oxygen species on the surface of the WO_3 nanostructures was O^{2-}. Thus, an electron depletion layer would be formed in the surface region of WO_3, leading to the increase of the resistance. Upon exposure to acetone, the O^{2-} can react with the acetone molecules, according to equation (4), which releases the electrons back to the conduction band of WO_3. As a result, the resistance of the WO_3 sensor decreased again.

$$CH_3COCH_3 + 8O^{2-}\ (\text{adsorbed}) \rightarrow 3CO_2 + 3H_2O\ (\text{adsorbed}) + 16e^- \quad (4)$$

As discussed above, the 2D WO_3 nanosheets derived from the IF-WS_2 nanoparticles exhibited highly enhanced acetone-sensing performance compared with the 0D WO_3 nanoparticles. This is because the 2D WO_3 nanosheets exhibited smaller sizes and more edges than the 0D WO_3 nanoparticles. As determined from the TEM analysis, the formation of the 2D WO_3 nanosheets arouse from the simultaneous oxidation and fracture of the IF-WS_2 nanoparticles, and one IF-WS_2 nanoparticle can produce a few pieces of WO_3 nanosheets. After the transformation, more active sites were generated for the adsorption of the O^{2-} and acetone molecules and for the reactions between them. As illustrated in Fig. 7b, the reactions between the O^{2-} and the acetone molecules took place mostly on the surfaces of the WO_3 nanoparticles. As for the 2D WO_3 nanosheets (Fig. 7c), the reactions may occur not only on their surfaces but also at the edges. As a result, more electrons were released back to the WO_3 nanosheets when exposed to acetone, resulting in a higher response.

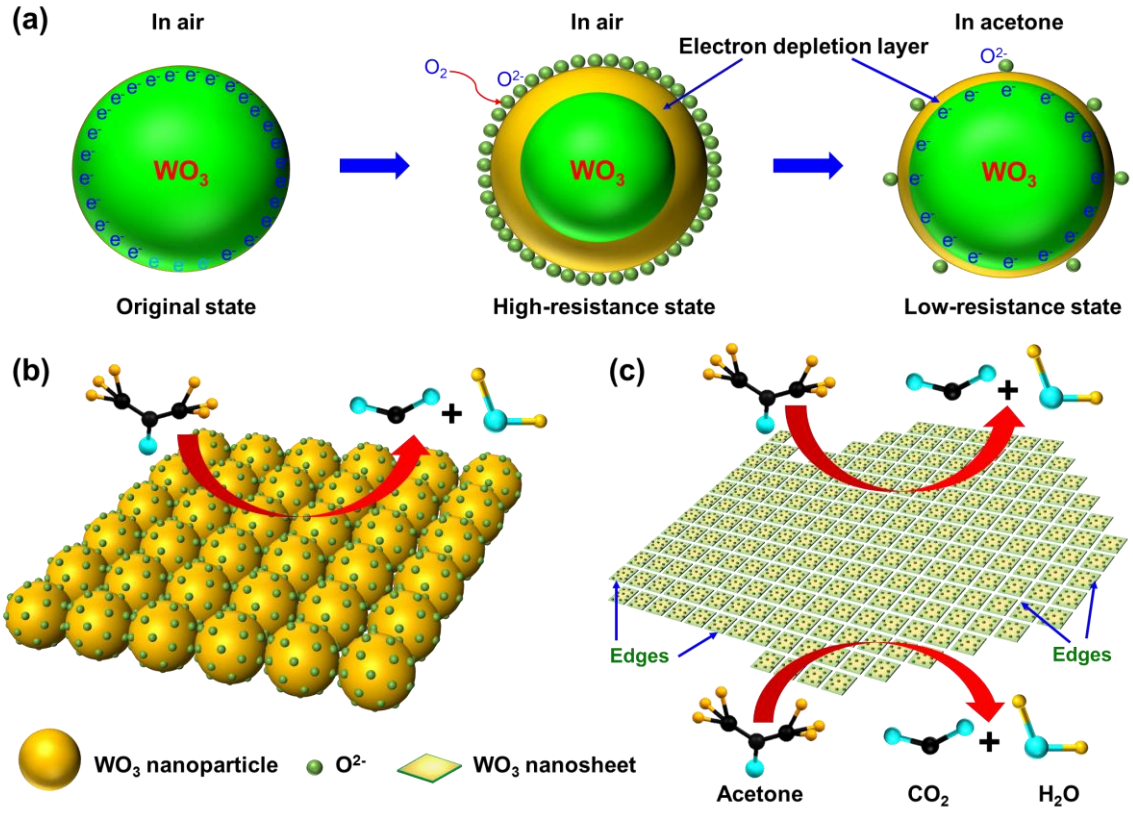

Fig. 7. (a) Schematic of acetone-sensing mechanism of WO_3. Schematics of reactions between oxygen ion species (O^{2-}) and acetone molecules on the surfaces of (b) WO_3 nanoparticles and (c) WO_3 nanosheets.

The annealing temperature could strongly influence the acetone-sensing performance of the annealed IF-WS_2 nanoparticles, and the WS_2-500 and WS_2-350 demonstrated the highest and lowest responses, respectively. Both the chemical compositions and microstructures of the annealed IF-WS_2 nanoparticles need to be considered for interpreting their acetone-sensing behaviors. When the annealing temperature was not higher than 450 ºC, the resulting samples were the WO_3/WS_2 heterostructures. It should be noted that the IF-WS_2 nanoparticles have very poor acetone-sensing ability because they showed negligible response to acetone at any operating temperature, which indicates that the presence of WS_2 were detrimental to the acetone-sensing performance of the resulting samples. As a result, the WS_2-350 with high amount of WS_2 showed the lowest response, despite of the formation of the WO_3/WS_2 heterostructures. Further increasing the annealing temperature to 400 ºC, a great number of WO_3 nanosheets were formed and only a very small amount of WS_2 remained in the resulting sample. Accordingly, the acetone-sensing performance was

significantly improved. After annealing at 450 ºC and 500 ºC, the IF-WS_2 nanoparticles was completely transformed to the tiny WO_3 nanosheets. Thus, both the WS_2-450 and WS_2-500 sensors showed high responses to acetone. Since the crystallinity of the WO_3 nanosheets increased with increasing annealing temperature, the WS_2-500 sensor exhibited slightly enhanced response compared with the WS_2-450 sensor. When the annealing temperature reached 550 ºC, however, coalescence of the resulting WO_3 nanosheets occurred, leading to the decreased acetone-sensing performance. Therefore, the response of the WS_2-550 sensor were lower than those of the WS_2-450 and WS_2-500 sensors. Overall, the increasing response order was WS_2-350 < WS_2-400 < WS_2-550 < WS_2-450 < WS_2-500 sensors.

4. Conclusions

By first creating 2D WO_3 nanosheets through a simple annealing of the IF-WS_2 nanoparticles in air, we further demonstrate their superb sensing function to acetone, with advanced features including low LOD, fast response, great stability and repeatability. The formation of 2D WO_3 from the IF-WS_2 precursors was accompanied by the collapse of the cages during annealing, resulting in 2D WO_3 nanosheets with lateral size of 40-80 nm, smaller than the precursors. The 2D WO_3 nanosheets exhibited high response (14.7 to 50 ppm of acetone), very low theoretical LOD (ppb level), good selectivity against other VOCs, fast response/recovery rates (6/9 s to 0.17 ppm acetone), promising repeatability (100 cycles), and reliable long-term stability (14 days). This new type of acetone sensors with sub-ppm level detection capacity and other characteristics are promising for applications in constructing portable devices for early diabetes diagnosis.

Acknowledgements

This work is financially supported by the International Science and Technology Cooperation Program (CU03-29), the Natural Science Foundation of Shanghai (17ZR1440900), the “Shuguang” Program of Shanghai Education Commission (19SG46), and the Shanghai Engineering Technology Research Centre of Deep Offshore Material (19DZ2253100).

References

[1] T.A. Popov, Human exhaled breath analysis, Ann. Allergy Asthma Immunol. 106 (2011) 451-6.

[2] C.E. Davis, M. Frank, B. Mizaikoff, H. Oser, The Future of Sensors and Instrumentation for Human Breath Analysis, IEEE Sens. J. 10 (2010) 3-6.

[3] M.Y. Chuang, C.C. Chen, H.W. Zan, H.F. Meng, C.J. Lu, Organic gas sensor with an improved lifetime for detecting breath ammonia in hemodialysis patients, ACS Sens. 2 (2017) 1788-95.

[4] M.Y. Chuang, Y.T. Lin, T.W. Tung, L.Y. Chang, H.W. Zan, H.F. Meng, et al., Room-temperature-operated organic-based acetone gas sensor for breath analysis, Sens. Actuators B Chem. 260 (2018) 593-600.

[5] Y.J. Su, J.J. Wang, B. Wang, T.N. Yang, B.X. Yang, G.Z. Xie, et al., Alveolus-inspired active membrane sensors for self-powered wearable chemical sensing and breath analysis, ACS Nano, 14 (2020) 6067-75.

[6] S. Yang, J. Sun, L. Xu, Q. Zhou, X. Chen, S. Zhu, et al., Au@ZnO functionalized three-dimensional macroporous WO3: A application of selective H2S gas sensor for exhaled breath biomarker detection, Sens. Actuators B Chem. 324 (2020) 128725.

[7] X. Huang, B. Li, L. Wang, X. Lai, H. Xue, J. Gao, Superhydrophilic, underwater superoleophobic, and highly stretchable humidity and chemical vapor sensors for human breath detection, ACS Appl. Mater. Inter. 11 (2019) 24533-43.

[8] Z. Wang, C. Wang, Is breath acetone a biomarker of diabetes? A historical review on breath acetone measurements, J. Breath Res. 7 (2013) 037109.

[9] C. Turner, Potential of breath and skin analysis for monitoring blood glucose concentration in diabetes, Expert Rev. Mol. Diagn. 11 (2011) 497-503.

[10] M. Storer, J. Dummer, H. Lunt, J. Scotter, F. McCartin, J. Cook, et al., Measurement of breath acetone concentrations by selected ion flow tube mass spectrometry in type 2 diabetes, J. Breath Res. 5 (2011) 046011.

[11] C.H. Deng, J. Zhang, X.F. Yu, W. Zhang, X.M. Zhang, Determination of acetone in human breath by gas chromatography-mass spectrometry and solid-phase microextraction with on-fiber derivatization, J. Chromatogr. B 810 (2004) 269-75.

[12] C. Turner, C. Walton, S. Hoashi, M. Evans, Breath acetone concentration decreases with blood glucose concentration in type I diabetes mellitus patients during hypoglycaemic clamps, J Breath Res.

3 (2009) 046004.

[13] W. Hu, Breath ethanol and acetone as indicators of serum glucose levels: An initial report, Ethnic Dis. 15 (2005) 32-4.

[14] K. Konigstein, S. Abegg, A.N. Schorn, I.C. Weber, N. Derron, A. Krebs, et al., Breath acetone change during aerobic exercise is moderated by cardiorespiratory fitness, J Breath Res. 15 (2020) 016006.

[15] B. Moser, F. Bodrogi, G. Eibl, M. Lechner, J. Rieder, P. Lirk, Mass spectrometric profile of exhaled breath-field study by PTR-MS, Resp. Physiol. Neurobiol. 145 (2005) 295-300.

[16] V. Ruzsanyi, J.I. Baumbach, S. Sielemann, P. Litterst, M. Westhoff, L. Freitag, Detection of human metabolites using multi-capillary columns coupled to ion mobility spectrometers, J. Chromatogr A 1084 (2005) 145-51.

[17] C. Wang, P. Sahay, Breath analysis using laser spectroscopic techniques: breath biomarkers, spectral fingerprints, and detection limits, Sensors (Basel) 9 (2009) 8230-62.

[18] D. Wang, F. Zhang, A. Prabhakar, X. Qin, E.S. Forzani, N. Tao, Colorimetric sensor for online accurate detection of breath acetone, ACS Sens. 6 (2021) 450–453.

[19] S. Zhang, M. Yang, K. Liang, A. Turak, B. Zhang, D. Meng, et al., An acetone gas sensor based on nanosized Pt-loaded Fe_2O_3 nanocubes, Sens. Actuators B Chem. 290 (2019) 59-67.

[20] Y. Zhong, W. Li, X. Zhao, X. Jiang, S. Lin, Z. Zhen, et al., High-response room-temperature NO_2 sensor and ultrafast humidity sensor based on SnO_2 with rich oxygen vacancy, ACS Appl. Mater. Inter. 11 (2019) 13441-9.

[21] Y. Gui, L. Yang, K. Tian, H. Zhang, S. Fang, P-type Co_3O_4 nanoarrays decorated on the surface of n-type flower-like WO_3 nanosheets for high-performance gas sensing, Sens. Actuators B Chem. 288 (2019) 104-12.

[22] X.W. Chen, S. Wang, C. Su, Y.T. Han, C. Zou, M. Zeng, et al., Two-dimensional Cd-doped porous Co_3O_4 nanosheets for enhanced room-temperature NO_2 sensing performance, Sens. Actuators B Chem. 305 (2019) 127393.

[23] D. Zhang, J. Wu, P. Li, Y. Cao, Z. Yang, Hierarchical nanoheterostructure of tungsten disulfide nanoflowers doped with zinc oxide hollow spheres: benzene gas sensing properties and

first-principles study, ACS Appl. Mater. Inter. 11 (2019) 31245-56.

[24] H. Yu, S. Gao, X. Cheng, P. Wang, X. Zhang, Y. Xu, et al., Morphology controllable Fe_2O_3 nanostructures derived from Fe-based metal-organic frameworks for enhanced humidity sensing performances, Sens. Actuators B Chem. 297 (2019) 126744.

[25] Z. Wang, S. Gao, T. Fei, S. Liu, T. Zhang, Construction of ZnO/SnO_2 heterostructure on reduced graphene oxide for enhanced nitrogen dioxide sensitive performances at room temperature, ACS Sens. 4 (2019) 2048-57.

[26] Y. Han, Y. Liu, C. Su, X. Chen, M. Zeng, N. Hu, et al., Sonochemical synthesis of hierarchical WO_3 flower-like spheres for highly efficient triethylamine detection, Sens. Actuators B Chem. 306 (2020) 127536.

[27] Y.H. Zhu, Y. Zhao, J.H. Ma, X.W. Cheng, J. Xie, P.C. Xu, et al., Mesoporous tungsten oxides with crystalline framework for highly sensitive and selective detection of foodborne pathogens, J. Am. Chem. Soc. 139 (2017) 10365-10373.

[28] S. Wei, S. Li, R. Wei, S. Liu, W. Du, Different morphologies of WO_3 and their exposed facets-dependent acetone sensing properties, Sens. Actuators B Chem. 329 (2020) 129188.

[29] V. Galstyan, N. Poli, A. D'Arco, S. Macis, S. Lupi, E. Comini, A novel approach for green synthesis of WO_3 nanomaterials and their highly selective chemical sensing properties, J. Mater. Chem. A 8 (2020) 20373-85.

[30] J. Lu, C. Xu, L. Cheng, N. Jia, J. Huang, C. Li, Acetone sensor based on WO_3 nanocrystallines with oxygen defects for low concentration detection, Mat. Sci. Semicon. Proc. 101 (2019) 214-22.

[31] M. Imran, S.S.A.A.H. Rashid, Y. Sabri, N. Motta, T. Tesfamichael, P. Sonar, et al., Template based sintering of WO_3 nanoparticles into porous tungsten oxide nanofibers for acetone sensing applications, J Mater. Chem. C 7 (2019) 2961-70.

[32] M.G. Stanford, K. Yang, Y. Chyan, C. Kittrell, J.M. Tour, Laser-induced graphene for flexible and embeddable gas sensors, ACS Nano 13 (2019) 3474-82.

[33] E. Salih, A.I. Ayesh, DFT investigation of H_2S adsorption on graphene nanosheets and nanoribbons: Comparative study, Superlattice. Microst. 146 (2020) 106650.

[34] Z. Yang, A. Liu, C. Wang, F. Liu, J. He, S. Li, et al., Improvement of gas and humidity sensing

properties of organ-like Mxene by alkaline treatment, ACS Sens. 4 (2019) 1261-9.

[35] E. Lee, A. VahidMohammadi, Y.S. Yoon, M. Beidaghi, D.J. Kim, Two-dimensional vanadium carbide MXene for gas sensors with ultrahigh sensitivity toward nonpolar gases, ACS Sens. (2019) 1603-11.

[36] W. Yuan, K. Yang, H. Peng, F. Li, F. Yin, A flexible VOCs sensor based on a 3D Mxene framework with a high sensing performance, J. Mater. Chem. A 6 (2018) 18116-24.

[37] J.-H. Kim, A. Mirzaei, H.W. Kim, S.S. Kim, Realization of Au-decorated WS_2 nanosheets as low power-consumption and selective gas sensors, Sens. Actuators B Chem. 296 (2019) 126659.

[38] Z. Yang, B.L. Li, Y.T. Han, C. Su, X.W. Chen, Z.H. Zhou, et al., Gas sensors based on two-dimensional transition metal dichalcogenide nanoheterojunctions (in Chinese), Chin. Sci. Bull. 64 (2019) 3699-3716.

[39] Y.T. Han, Y. Liu, C. Su, X.W. Chen, B.L. Li, W.K. Jiang, et al., Hierarchical WS_2-WO_3 nanohybrids with p-n heterojunctions for NO_2 detection, ACS Appl. Nano Mater. 4 (2021) 1626-1634.

[40] Y. Kim, K.C. Kwon, S. Kang, C. Kim, T.H. Kim, S.P. Hong, et al., Two-dimensional NbS_2 gas sensors for selective and reversible NO_2 detection at room temperature, ACS Sens. 4 (2019) 2395-402.

[41] H.K. Adigilli, B. Padya, L. Venkatesh, V.S.K. Chakravadhanula, A.K. Pandey, J. Joardar, Oxidation of 2D-WS_2 nanosheets for generation of 2D-WS_2/WO_3 heterostructure and 2D and nanospherical WO_3, Phys. Chem. Chem. Phys. 21 (2019) 25139-47.

[42] A. Azam, J. Kim, J. Park, T.G. Novak, A.P. Tiwari, S.H. Song, et al., Two-dimensional WO_3 nanosheets chemically converted from layered ws2 for high-performance electrochromic devices, Nano Lett. 18 (2018) 5646-51.

[43] D. Yim, F. Raza, J.H. Park, J.H. Lee, H.I. Kim, J.K. Yang, et al., Ultrathin WO_3 nanosheets converted from metallic WS2 Sheets by spontaneous formation and deposition of PdO nanoclusters for visible light-driven C-C coupling reactions, ACS Appl. Mater. Inter. 11 (2019) 36960-9.

[44] F. Perrozzi, S.M. Emamjomeh, V. Paolucci, G. Taglieri, L. Ottaviano, C. Cantalini, Thermal stability of WS_2 flakes and gas sensing properties of WS_2/WO_3 composite to H_2, NH_3 and NO_2, Sens.

Actuators B Chem. 243 (2017) 812-22.

[45] Y.Q. Zhu, T. Sekine, Y.H. Li, W.X. Wang, M.W. Fay, H. Edwards, et al., WS_2 and MoS_2 inorganic fullerenes-super shock absorbers at very high pressures, Adv. Mater. 17 (2005) 1500-3.

[46] L. Rapoport, Yu. Bilik, Y. Feldman, M. Homyonfer, S. R. Cohen, R. Tenne, Hollow nanoparticles of WS_2 as potential solid-state lubricants, Nature 387 (1997) 791-793.

[47] F. Xu, T.P. Almeida, H. Chang, Y.D. Xia, M.L. Wears, Y.Q. Zhu, Multi-walled carbon/IF-WS_2 nanoparticles with improved thermal properties, Nanoscale 5 (2013) 10504-10.

[48] F. Xu, N. Wang, H. Chang, Y. Xia, Y. Zhu, Continuous production of IF-WS_2 nanoparticles by a rotary process, Inorganics 2 (2014) 313-33.

[49] R. Tenne, M. Homyonfer, Y. Feldman, Nanoparticles of layered compounds with hollow cage structures (inorganic fullerene-like structures), Chem. Mater. 10 (1998) 3225-3238.

[50] S.H. Song, B.H. Kim, D.H. Choe, J. Kim, D.C. Kim, D.J. Lee, et al., Bandgap widening of phase quilted, 2D MoS_2 by oxidative intercalation, Adv. Mater. 27 (2015) 3152-8.

[51] N. Zhang, C. Chen, Z. Mei, X. Liu, X. Qu, Y. Li, et al., Monoclinic tungsten oxide with {100} facet orientation and tuned electronic band structure for enhanced photocatalytic oxidations, ACS Appl. Mater. Inter. 8 (2016) 10367-74.

[52] P.M. Oliver, S.C. Parker, R.G. Egdell, F.H. Jones, Computer simulation of the surface structures of WO_3, J. Chem. Soc. Faraday Trans. 92 (1996) 2049-2056.

[53] M. Li, E.I. Altman, A. Posadas, C.H. Ahn, The p(4 × 2) surface reconstruction on epitaxial WO_3 thin films, Surf. Sci. 542 (2003) 22-32.

[54] L.Y. Zhu, K.P. Yuan, J.G. Yang, H.P. Ma, T. Wang, X.M. Ji, et al., Fabrication of heterostructured p-CuO/n-SnO_2 core-shell nanowires for enhanced sensitive and selective formaldehyde detection, Sens. Actuators B Chem. 290 (2019) 233-241.

[55] M. Yin, S. Liu, Controlled ZnO hierarchical structure for improved gas sensing performance, Sens. Actuators B Chem. 209 (2015) 343-51.

[56] C. Liu, H. Lu, J. Zhang, J. Gao, G. Zhu, Z. Yang, et al., Crystal facet-dependent p-type and n-type sensing responses of TiO_2 nanocrystals, Sens. Actuators B Chem. 263 (2018) 557-67.

[57] N. Hongsith, E. Wongrat, T. Kerdcharoen, S. Choopun, Sensor response formula for sensor

based on ZnO nanostructures, Sens. Actuators B Chem. 144 (2010) 67-72.

[58] K. Yuan, C.Y. Wang, L.Y. Zhu, Q. Cao, J.H. Yang, X.X. Li, et al., Fabrication of a micro-electromechanical system-based acetone gas sensor using CeO_2 nanodot-decorated WO_3 nanowires, ACS Appl. Mater. Inter. 12 (2020) 14095-104.

[59] Z.H. Wang, J. Xue, D.M. Han, F.B. Gu, Controllable defect redistribution of ZnO nanopyramids with exposed {10-11} facets for enhanced gas sensing performance, ACS Appl. Mater. Inter. 7 (2015) 308-17.

[60] S. Sun, M. Wang, X. Chang, Y. Jiang, D. Zhang, D. Wang, et al., $W_{18}O_{49}/Ti_3C_2T_x$ Mxene nanocomposites for highly sensitive acetone gas sensor with low detection limit, Sens. Actuators B Chem. 304 (2020) 127274.

[61] T. Zhou, R. Zhang, Y. Wang, T. Zhang, MOF-Derived 1 D α-$Fe_2O_3/NiFe_2O_4$ heterojunction as efficient sensing materials of acetone vapors, Sens. Actuators B Chem. 281 (2019) 885-92.

[62] D. Wang, S. Huang, H. Li, A. Chen, P. Wang, J. Yang, et al., Ultrathin WO_3 nanosheets modified by g-C_3N_4 for highly efficient acetone vapor detection, Sens. Actuators B Chem. 282 (2019) 961-71.

[63] Y. Li, Z. Hua, Y. Wu, Y. Zeng, Z. Qiu, X. Tian, et al., Modified impregnation synthesis of Ru-loaded WO_3 nanoparticles for acetone sensing, Sens. Actuators B Chem. 265 (2018) 249-56.

[64] R. Zhang, T. Zhou, L. Wang, T. Zhang, Metal-organic frameworks-derived hierarchical Co_3O_4 structures as efficient sensing materials for acetone detection, ACS Appl. Mater. Inter. 10 (2018) 9765-73.

[65] J. Huang, Q. Wan, Gas sensors based on semiconducting metal oxide one-dimensional nanostructures, Sensors 9 (2009) 9903-9924.

[66] V. Dua, S.P. Surwade, S. Ammu, S.R. Agnihotra, S. Jain, K.E. Roberts, et al., All-organic vapor sensor using inkjet-printed reduced graphene oxide, Angew. Chem. Int. Edit. 122 (2010) 2200-2203.

[67] W.T. Honeycutt, M.T. Ley, N.F. Materer, Precision and limits of detection for selected commercially available, low-cost carbon dioxide and methane gas sensors, Sensors 19 (2019) 3157.

[68] X.R. Zhang, B. Dong, W. Liu, X.Y. Zhou, M. Liu, X.K. Sun, et al., Highly sensitive and selective acetone sensor based on three-dimensional ordered WO_3/Au nanocomposite with enhanced performance, Sens. Actuators B Chem. 320 (2020) 128405.

[69] Y. Xu, T. Ma, L. Zheng, Y. Zhao, X. Liu, J. Zhang, Heterostructures of hematite-sensitized $W_{18}O_{49}$ hollow spheres for improved acetone detection with ultralow detection limit, Sens. Actuators B Chem. 288 (2019) 432-41.

[70] J.Y. Shen, L. Zhang, J. Ren, J.C. Wang, H.C. Yao, Z.J. Li, Highly enhanced acetone sensing performance of porous C-doped WO_3 hollow spheres by carbon spheres as templates, Sens. Actuators B Chem. 239 (2017) 597-607.

[71] Y. Ren, Y. Zou, Y. Liu, X. Zhou, J. Ma, D. Zhao, et al., Synthesis of orthogonally assembled 3D cross-stacked metal oxide semiconducting nanowires, Nat. Mater. 19 (2020) 203-11.

[72] C. Wang, Y.L. Wang, P.F. Cheng, L.P. Xu, F. Dang, T.L. Wang, et al., In-situ generated TiO_2/α-Fe_2O_3 heterojunction arrays for batch manufacturing of conductometric acetone gas sensors, Sens. Actuators B Chem. 338 (2021) 129851.